Density-Wave States in Twisted Double-Bilayer Graphene

Peter Rickhaus,[1,*] Folkert K. de Vries,[1] Jihang Zhu,[2] Elías Portolés,[1] Giulia Zheng,[1] Michele Masseroni,[1] Annika Kurzmann,[1] Takashi Taniguchi,[3] Kenji Wantanabe,[3] Allan H. MacDonald,[2] Thomas Ihn,[1] and Klaus Ensslin[1]

[1] *Solid State Physics Laboratory, ETH Zürich, CH-8093 Zürich, Switzerland*
[2] *Department of Physics, University of Texas at Austin, Austin, Texas 78712, USA*
[3] *National Institute for Material Science, 1-1 Namiki, Tsukuba 305-0044, Japan*

(Dated: May 20, 2020)

When twisted to angles near 1°, graphene multilayers provide a new window on electron correlation physics by hosting gate-tuneable strongly-correlated states, including insulators, superconductors, and unusual magnets. Here we report the discovery of a new member of the family, density-wave states, in double bilayer graphene twisted to 2.37°. At this angle the moiré states retain much of their isolated bilayer character, allowing their bilayer projections to be separately controlled by gates. We use this property to generate an energetic overlap between narrow isolated electron and hole bands with good nesting properties. Our measurements reveal the formation of ordered states with reconstructed Fermi surfaces, consistent with density-wave states, for equal electron and hole densities. These states can be tuned without introducing chemical dopants, thus opening the door to a new class of fundamental studies of density-waves and their interplay with superconductivity and other types of order, a central issue in quantum matter physics.

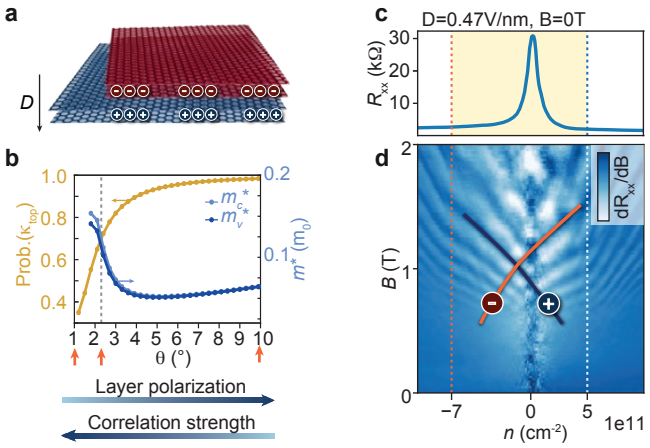

FIG. 1. **Designed density-wave state in a moiré double bilayer.** a) Applying an electric field D to twisted double bilayer graphene will charge the top/bottom bilayer with electrons/holes. b) The layer polarization is given by Prob($\kappa_{\rm top}$) and the correlation strength scales with the effective mass m^*. Prob($\kappa_{\rm top}$)(θ) and $m^*(\theta)$ (at layer energy difference $\Delta_{\rm V} = 40\,$meV, see below) are obtained from band structure calculations, showing that twists around $\theta = 2.37°$ combine strong polarizations and large masses and are favorable for DW formation. The red arrows mark twist angles at which measurements in the SI, section C are presented. A correlated electron/hole gap is seen only at an intermediate θ. c) A peak in $R_{\rm xx}$ occurs at $D = 0.47\,$V/nm and $n = 0$, in a TDBG device with $\theta = 2.37°$, and is consistent with a thermally activated gap (see SI section D). d) The bilayer's Landau-fan diagram demonstrates that the gap appears inside a regime with both electron and hole bands, as testified by the presence of Shubnikov-de Haas resistance peaks (orange and blue) that have opposite n *vs.* B slopes.

One Sentence Summary: We report the discovery of a density-wave state in twisted double bilayer graphene.

Fermi surface nesting refers to electron and hole Fermi surfaces that map onto each other under translation by a nesting wavevector $\vec{Q}$. Because nesting implies a small band energy cost for coherent superposition between electrons and holes, it favors interaction-driven broken symmetry states. The nesting condition ($\epsilon(\vec{k}_{\rm F} + \vec{Q}) = -\epsilon(\vec{k}_{\rm F})$),where epsilon is a small energy offset from the Fermi energy) implies[1] that if two closed Fermi surfaces are perfectly nested, they enclose the same area. Mixing two Fermi surfaces nested by wavevector $\vec{Q}$ leads to density-wave (DW) order with wavelength $2\pi/Q$. In the seminal theoretical work on DW states by Peierls[2], nesting occurs between like-spins in half-filled bands, the interactions are lattice mediated, and the DW is accompanied by a lattice distortion. The Peierls transition is one of the first instabilities of the metallic state to be recognized, and has been observed in a large range of materials. DW states can also be favored by Coulomb interactions between electrons, in which case the lattice distortions[3] play a parasitic role only. The DW is then often referred to as an excitonic insulator[4]. This term is suggested by viewing the order as a condensation of bosonic electron/hole pair states. Evidence for equilibrium excitonic condensation has been reported in 1T-$TiSe_2$[5], in Sb nanoflakes[3] and in double quantum wells at high magnetic fields[6,7]. Condensation of non-equilibrium excitons and polaritons in optically pumped electron-hole fluids has also been studied extensively.[8] DWs continue to attract attention due to their rich intrinsic physics and their close relationship to superconductivity[9].

Twisting Van der Waals (VdW) materials, including graphene bilayers (TBG)[10–15] and double Bernal bilayers (TDBG)[16–22], is a proven strategy to engineer moiré bands that favor strongly correlated electronic states. In the present work we seek to realize DW physics by designing a moiré material with electron/hole bands that are both nested and relatively narrow. To this end we have studied the properties of TDBG[16–22] at intermediate twist angles, where the layer coupling is strong enough to form moiré bands, but weak enough to retain the polarizability of decoupled bilayers[23–26]. This polarizability can be quantified by the probability Prob($\kappa_{\rm top}$) to find a band state at the κ-point (of the mini-Brillouin zone) in the upper bilayer. If Prob($\kappa_{\rm top}$) is large, which is the case at large twist angles, applying a displacement field D will charge the top bilayer with electrons and the bottom bilayer with holes (Fig. 1a). But DW states are fragile and if they occur, only indirectly observable[25]. Thus the correlation strength needs to be maximized by approaching smaller angles where the narrowed moiré bands have a larger effective mass m^* (Fig. 1b).

Here we show that DW states are favored to form close to $\theta = 2.37°$, in the intermediate twist angle regime. Figs. 1cd summarize the main experimental findings. We observe a resistance peak at zero total density $n = 0$ and displacement field $D = 0.47\,$V/nm (Fig. 1c) which appears when electrons and holes with approximately the same density coexist. This coexistence is evident in Landau-fan measurements (Fig. 1d) that reveal electron and hole

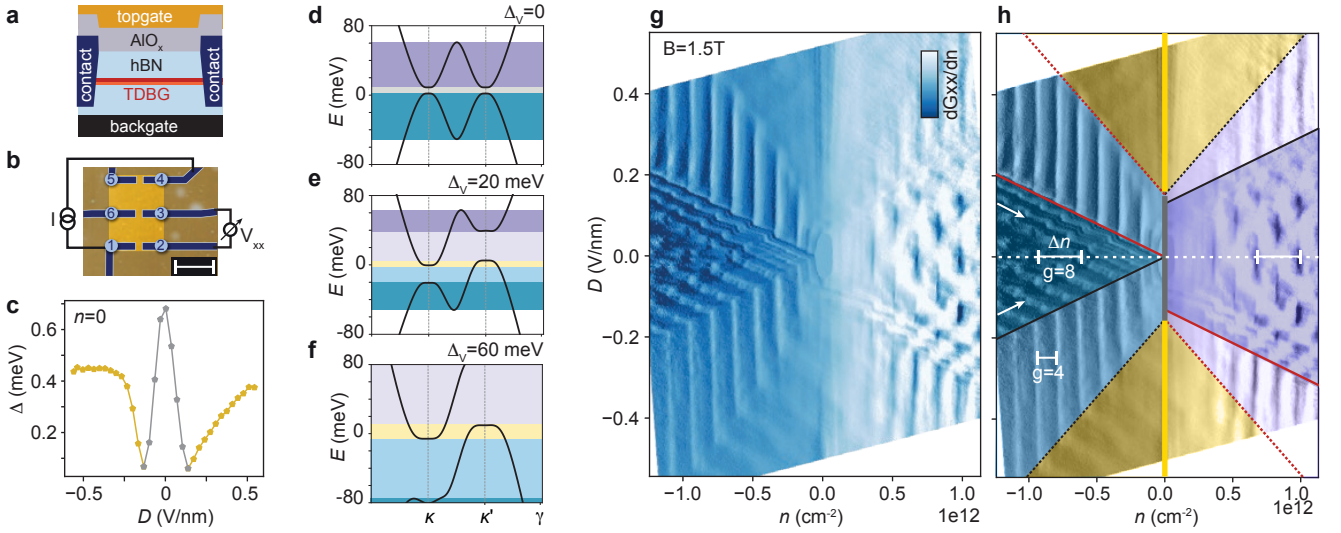

FIG. 2. **Establishing electron/hole fluids**. a) Side view and b) top view of the stack. $R_{xx} \equiv V_{23}/I_{14}$. Scale-bar: $2\,\mu$m. c) From thermal activation measurements we obtain $\Delta(D)$. d)-f) Single-particle band structures for different $\Delta_V \propto D$. g) $\partial/\partial n\,(1/R_{xx})(D,n)$ at $B = 1.5\,\mathrm{T}$ exhibits SdH oscillations that distinguish the regions highlighted in h). In the yellow region, electrons and holes coexist.

minibands which cross in energy. In this report, we first discuss how these overlapping electron/hole regions are formed by tuning D and n and then show how Fermi surface nesting is influenced by these parameters. In a next step, we support our interpretation by Hartree-Fock (HF) simulations. Finally, we discuss that a parallel magnetic field lifts the spin and a perpendicular field the valley degeneracy of the DW state, allowing to address its spin or valley symmetry.

We now discuss our device in more detail by showing a side view schematic in Fig. 2a. We tune the density $n = (C_t V_t + C_b V_b)/e$ and displacement field $D = (C_b V_b - C_t V_t)/2\epsilon_0$ by applying voltages V_t and V_b to top and back gate electrodes. Here, C_t, C_b are the corresponding capacitances per unit area. The resistance peak in Fig. 1c is measured using the contact geometry in Fig. 2b.

From the decrease of the resistance peak with increasing temperature we extract a gap Δ using the Arrhenius law $R_{xx} \propto \exp(\Delta/2k_BT)$. The extracted dependence of Δ on D at total denstiy $n = 0$ is shown in 2c. The data reveals a gap around $D = 0$ (gray line) that closes with increasing $|D|$. Another gap is opened at large $|D|$ (yellow line). We compare this finding to single-particle band structure calculations in Fig. 2d-f for different layer on-site energy differences Δ_V ($\Delta_V \approx bD$ with $b \approx 59\,\mathrm{meV/(Vnm^{-1})}$ see SI, section A). For $\Delta_V = 0$ (Fig. 2d), a gap is present at $E = 0$ allowing to assign a single-particle origin to Δ around $|D| = 0$ (gray line in Fig. 2c)[27]. For increasing Δ_V (and D), the single-particle band structure is not gapped anymore (Fig. 2ef). This indicates that the measured Δ at large $|D|$ (yellow line) originates from a correlated state formed out of electrons at the κ and holes at the κ' point.

In the following we present measurements of Shubnikov-de Haas (SdH) oscillations for different n and D. In Figs. 2gh we plot the numerical derivative of the inverse resistance $\partial/\partial n\,(1/R_{xx})$ (this quantity is chosen for best visibility of relevant features) measured in a perpendicular magnetic field $B_\perp = 1.5\,\mathrm{T}$. Along the dashed line at $D = 0$ in Fig. 2h, the spacing between SdH oscillations corresponds to the band degeneracy $g = 8$. The degeneracy is lifted by changing D and SdH lines with two slopes emerge (indicated with arrows) in the dark blue and the dark purple region. In the light blue and light purple region, the pattern changes and lines with $g = 4$ that are parallel to the $n = 0$ line are seen. The slope of the SdH lines then changes again in the yellow region, and the oscillations become weaker.

These observations can be explained by the single-particle band structures shown in Fig. 2d-f. At $\Delta_V = 0$ (Fig. 2d) two separate Fermi surfaces of the four-fold spin/valley degenerate bilayer graphene emerge near the κ and κ' points, leading to a degeneracy $g = 8$. Changing Δ_V (or D) breaks the layer degeneracy and the SdH lines acquire two distinct slopes. These correspond to states in the top and bottom bilayer, thereby demonstrating that charge carriers in these bilayers can be tuned independently[26,28]. With Δ_V, single-band regions (light blue, light purple in Fig. 2e and f) with $g = 4$ emerge, where the Fermi surface area is proportional to total density n. Around charge neutrality (yellow) bands with opposite carrier type coexist. The region boundaries are well described using an electrostatic model (see SI section H and G) where we also discuss the observed asymmetry with respect to n. We conclude that the SdH measurements agree with the band structure calculation and that we observe a region where electron/hole bands overlap. In this region, at $n = 0$, a correlated gap emerges.

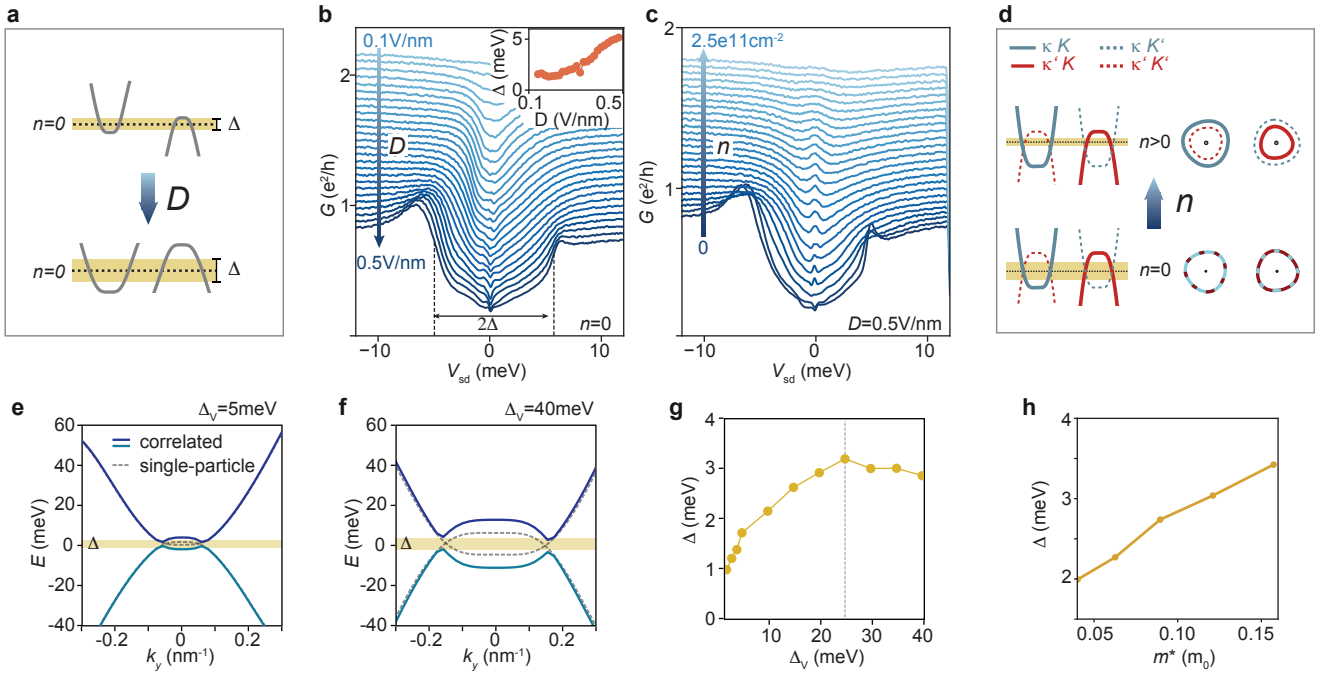

FIG. 3. **Nesting**. a) The size of Fermi surfaces at $n = 0$ and masses m^* increase with D. b) $G(V_{\rm sd}, D)$ measurements reveals the appearance of a gap Δ. Curves are offset from the $D = 0.47\,\mathrm{V/nm}$ trace. The inset shows extracted $\Delta(D)$, revealing that Δ increases with D. c) $G(V_{\rm sd}, n)$ at $D = 0.47\,\mathrm{V/nm}$ showing that the gap vanishes with increasing n, where d) Fermi surface nesting falters. Depicted is the calculated dispersion and Fermi surface around κ (blue) and κ' (red) in the K (solid) and K' (dashed) valley. For details, see SI section F. e) Single-particle (dashed) and HF (solid) bands at $\Delta_{\rm V} = 5\,\mathrm{meV}$ and f) $\Delta_{\rm V} = 40\,\mathrm{meV}$. g) From HF calculations, we obtain $\Delta(\Delta_{\rm V})$ and reproduce the experimental observations. h) Δ strongly depends on m^*.

We now discuss the dependence of the correlated gap on the parameters D and n which change the sizes and symmetries of the Fermi surfaces. When increasing D, the Fermi surfaces at $n = 0$ and the effective masses increase as sketched in Fig. 3a. We expect that this stabilizes the DW state. Indeed, and in agreement with thermal activation measurements, the two-terminal conductance as a function of DC bias $G(V_{\rm sd})$ traces in Fig. 3b reveal that Δ increases with D. In the inset of Fig. 3b we show the increase of Δ with D in orange dots which we compare to Hartree-Fock (HF) calculations later. At $D = 0.47\,\mathrm{V/nm}$ and $n = 0$, $\Delta \approx 5\,\mathrm{meV}$ (Δ is determined by the inflection points). We note that usually, thermal activation energy and the bias gap agree, but differ by an order of magnitude here. We speculate that this originates from complex thermal breakdown of the correlated gap and estimate that the bias measurement overestimates Δ by $\sim 10\%$ by additional series resistances (see SI section A).

In Fig. 3c we show the evolution of $\Delta(n)$ at $D = 0.47\,\mathrm{V/nm}$. Upon increasing n, the gap smears out and vanishes at $n \approx 2.5 \times 10^{11}\,\mathrm{cm}^{-2}$. Tuning to finite n introduces an asymmetry between the electron and hole Fermi surfaces (blue and red), as depicted in Fig. 3d. As a consequence, nesting will become less favorable and unpaired charge carriers (electrons for $n > 0$) contribute to the background conductance. These effects lead to shrinking and smearing of the gap. Note that Fermi surfaces in the same valley are asymmetric even at $n = 0$ as they are not perfectly circular due to interlayer tunneling between the middle two layers. However, the Fermi surfaces of opposite valleys K and K' (solid and dashed) match, suggesting that the correlated state is formed out of charge carriers from opposite valleys.

We confirm the gap opening in HF calculations where we incorporate the Coulomb potential and calculate Δ self-consistently (see SI section L). We obtain the correlated bands as shown in Fig. 3ef. A gap is opened by electron-hole correlation, and linearly increases with layer on-site energy difference Δ_V for $\Delta_V \leq 25$ meV. Both the gap size and the linearity with respect to displacement field agree with experiments, as shown in Fig. 3g. We point out that this behavior is a result of decreasing static dielectric constant $\epsilon(\mathbf{q})$ with D (see SI section M). For $\Delta_V > 25$ meV, the gap decreases as a result of the non-negligible moiré band asymmetry (seen in Fig. 3f).

Our model allows us to adjust the interlayer hopping parameter γ_1 between dimer sites in each bilayer in order to change m^*. We observe an almost linear increase $\Delta(m^*)$ (see Fig. 3h), supporting our previous statement that m^* determines the correlation strength (Fig. 1b). Theory does not show a strong dependence of pairing on the momentum difference between Fermi surfaces, only on the effective mass. This agrees with the excitonic character of the DW.

While the spin degree of freedom is irrelevant for the formation of a correlated state when no magnetic field is

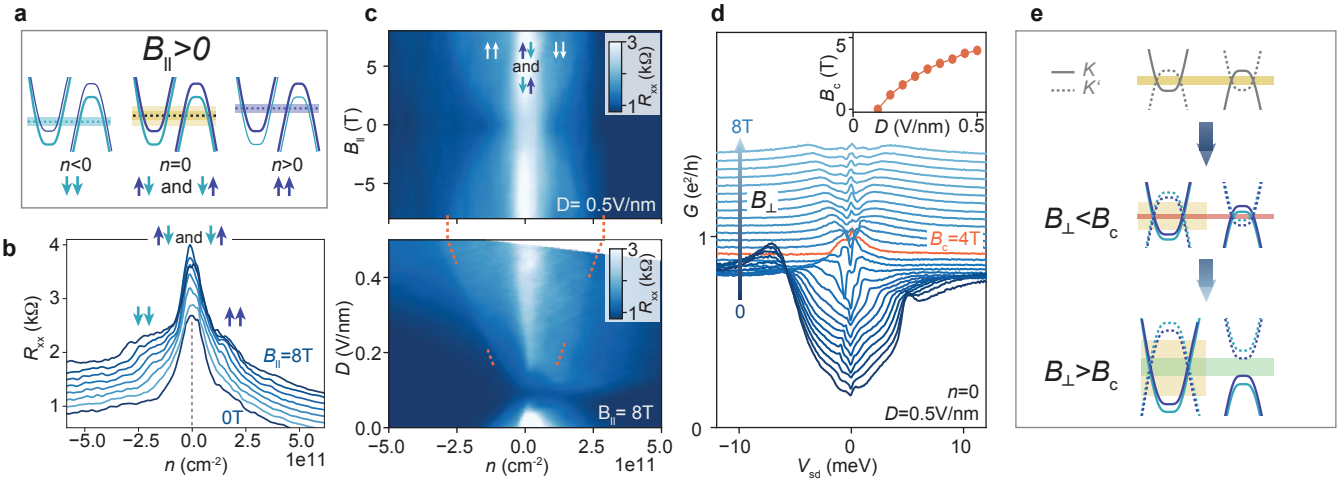

FIG. 4. **Spin polarized correlated gap.** a) Application of $B_\parallel$ splits the bands according to their magnetic moments, giving rise to regions where only one of the split bands is gapped. The arrows indicate the magnetic moments of the charge carriers. b) The partially gapped regions lead to an increase in R_{xx} at finite n. c) $R_{xx}(B_\parallel, n, D = 0.47\,\mathrm{V/nm})$ and $R_{xx}(D, n, B_\parallel = 8\,\mathrm{T})$ maps. The orange lines are calculated using $\Delta(D)$ and m^* from the experiment, without fitting parameters. d) The gap is closed by $B_\perp$. In the inset we plot the critical field, B_c, as a function of D. e) DW gaps are formed out of K (solid) and K' (dashed) bands which shift in $B_\perp$. Colors refer to Zeeman split spin bands, see a).

applied, the situation changes at a finite parallel field, $B_\parallel$, where the bands are split by the Zeeman energy. In Fig. 4a we depict the situation at finite $B_\parallel$, showing that perfect nesting (equal Fermi surface) between *opposite* magnetic moments is possible at $n = 0$, whereas perfect nesting between *same* magnetic moments is possible at $n \neq 0$. Therefore, by changing n we influence the spin state of the electron-hole pairs. Measured $R_{xx}(n, B_\parallel)$ traces are consistent with this concept (Fig. 4b). At $B_\parallel = 8\,\mathrm{T}$, a shoulder in resistance at finite n emerges, agreeing with a partially gapped bandstructure where half of the carriers form a correlated state while the other magnetic moment-bands remain conducting. How the region of enhanced conductance changes as a function of $|B_\parallel|$ and D can be observed in Fig. 4c. By using a basic model we calculate the expected density of the spin-polarized region as a function of displacement field and at large $B_\parallel$. The results are plotted with dashed lines in Fig. 4c and the model is discussed in SI section I and J. Good agreement between theory and experiment is found.

In Fig. 4d we show $G(V_{sd}, D = 0.47\,\mathrm{V/nm})$ traces in perpendicular magnetic fields $B_\perp$. The gap is closed at $B_c = 4\,\mathrm{T}$ (orange trace). The inset shows the extracted dependence $B_c(D)$. In a semi-classical picture, the bands shift with $B_\perp$ due to the Valley-Zeeman effect (Fig. 4e). The valley g-factor in bilayer graphene can range between $g_v \sim 20 - 120$[29] but is always much larger than the spin g-factor. Thus, for opposite valley pairing (K,K') the gap size at κ (yellow) increases with $B_\perp$ and decreases at κ' (red). G decreases most drastically if both bands are gapped. Thus, the gap closing in Fig. 4e with increasing $B_\perp$ and decreasing D can be viewed as the closing gap at κ' (red). For $B_\perp > B_c$ another gap opens (green), that can be interpreted as a single-particle gap at κ' (green in Fig. 4e) and a correlated gap at κ, i.e. the formation of a minivalley polarized DW. We note that a more rigorous analysis is required, taking into account the formation of Landau levels, especially for the regime where the magnetic length is smaller than the moiré periodicity. In Fig. 3c and Fig. 4d we observe a zero bias peak when applying a certain n or when passing B_c. The origin of this peak is currently not understood .

In conclusion, we have revealed the appearance of a correlated gap in TDBG at $\theta = 2.37°$, formed out of electrons and holes with equal Fermi surface. The wavefunctions in the top/bottom bilayer can be tuned individually making it possible to enter a region where electron and hole bands coexist. In this region, we observe a gap emerging from nesting of electron and hole Fermi surfaces. The spin and valley dependence of electron-hole pairing are both strongly influenced by the application of a magnetic field. The correlated electron/hole state can be viewed as an excitonic insulator and is expected to exhibit counterflow superfluidity. Quantum phase transitions between DWs and disordered states can be controlled without chemical doping by varying n, or by varying D at $n = 0$, and if continuous could provide a new window on non-Fermi-liquid physics.

* peterri@phys.ethz.ch

[1] D. I. Khomskii, *Basic Aspects of The Quantum Theory of Solids* (Cambridge University Press, Cambridge, 2010).
[2] R. Peierls, *Ann. Phys.* **396**, 121 (1930).
[3] Z. Li, *et al.*, *Nano Lett.* **19**, 4960 (2019).
[4] D. Jérome, T. M. Rice, W. Kohn, *Phys. Rev.* **158**, 462 (1967).
[5] A. Kogar, *et al.*, *Science* **358**, 1314 (2017).
[6] I. B. Spielman, J. P. Eisenstein, L. N. Pfeiffer, K. W. West, *Phys. Rev. Lett.* **84**, 5808 (2000).
[7] L. Du, *et al.*, *Nat. Commun.* **8**, 1 (2017).
[8] H. Deng, H. Haug, Y. Yamamoto, *Rev. Mod. Phys.* **82**, 1489 (2010).
[9] J. Chang, *et al.*, *Nat. Phys.* **8**, 871 (2012).
[10] Y. Cao, *et al.*, *Phys. Rev. Lett.* **117**, 116804 (2016).
[11] Y. Cao, *et al.*, *Nature* **556**, 43 (2018).
[12] A. L. Sharpe, *et al.*, *Science* **365**, 605 LP (2019).
[13] M. Yankowitz, *et al.*, *Science* **363**, 1059 (2019).
[14] P. Stepanov, *et al.*, *arXiv:1911.09198* (2019).
[15] Y. Saito, J. Ge, K. Watanabe, T. Taniguchi, A. F. Young, *arXiv:1911.13302* (2019).
[16] M. Koshino, *Phys. Rev. B* **99**, 235406 (2019).
[17] N. R. Chebrolu, B. L. Chittari, J. Jung, *Phys. Rev. B* **99**, 235417 (2019).
[18] Y. W. Choi, H. J. Choi, *Phys. Rev. B* **100**, 201402 (2019).
[19] X. Liu, *et al.*, *arXiv:1903.08130* (2019).
[20] C. Shen, *et al.*, *Nat. Phys.* (2020).
[21] G. W. Burg, *et al.*, *Phys. Rev. Lett.* **123**, 197702 (2019).
[22] M. He, *et al.*, *arXiv:2002.08904* (2020).
[23] A. Luican, *et al.*, *Phys. Rev. Lett.* **106**, 126802 (2011).
[24] J. D. Sanchez-Yamagishi, *et al.*, *Phys. Rev. Lett.* **108**, 76601 (2012).
[25] G. W. Burg, *et al.*, *Phys. Rev. Lett.* **120**, 177702 (2018).
[26] F. K. de Vries, *et al.*, *arXiv:2002.05267* (2020).
[27] P. Rickhaus, *et al.*, *Nano Lett.* **19**, 8821 (2019).
[28] P. Rickhaus, *et al.*, *Sci. Adv.* **6** (2020).
[29] Y. Lee, *et al.*, *Phys. Rev. Lett.* **124**, 126802 (2020).
[30] K. Kim, *et al.*, *Nano Lett.* **16**, 1989 (2016).
[31] A. A. Zibrov, *et al.*, *Nature* **549**, 360 (2017).
[32] L. Wang, *et al.*, *Science* **342**, 614 (2013).
[33] F. Haddadi, Q. Wu, A. J. Kruchkov, O. V. Yazyev, *Nano Lett.* **20**, 2410 (2020).
[34] H. Feshbach, *Ann. Phys.* **5**, 357 (1958).
[35] P. Löwdin, *J. Math.l Phys.* **3**, 969 (1962).

ACKNOWLEDGEMENTS

We acknowledge financial support from the European Graphene Flagship, the Swiss National Science Foundation via NCCR Quantum Science. P. Rickhaus acknowledges financial support from the ETH Fellowship program. Growth of hexagonal boron nitride crystals was supported by the Elemental Strategy Initiative conducted by MEXT, Japan and the CREST (JPMJCR15F3), JST. AHM and JZ were supported by the National Science Foundation through the Center for Dynamics and Control of Materials, an NSF MRSEC under Co- operative Agreement No. DMR-1720595 and by the Welch Foundation under grant TBF1473.

SUPPORTING INFORMATION

A. Fabrication, geometry and twist angle

We fabricate encapsulated TDBG by the tear-and-stack method[30]. Twisted double bilayer graphene is encapsulated in a top/bottom hBN with thicknesses 27.0/50.3 nm and features a graphite back gate[31]. Clean device areas are identified by atomic force microscopy. TDBG is contacted by edge contacts[32] (blue in the schematic in Fig. 2a). After deposition of local top gates (not shown in the schematic), the TDBG is etched (brown in the top-view in Fig. 2b) and 30 nm of AlO_x are deposited. Finally, we evaporate a global top gate (yellow). Throughout the measurements, the local and global top gates are tuned such that a uniform potential forms, therefore we will not discuss the effect of the local gate.

We measure R_{xx} by passing an AC current between contacts 1 and 4 (Fig. 2b), and measuring the voltage V_{xx} between contacts 2 and 3. For the finite bias measurements in Fig. 3 we apply AC+DC voltage between contacts 3 and 6 and measure the resulting AC current to obtain the differential conductance $G(V_{\mathrm{sd}})$. We have measured all other devices (3x6 contacts) on the stack and obtained comparable results, shown in section B. All measurements are performed at a temperature of 100 mK, unless stated otherwise.

For the measurement of $\Delta(V_{\mathrm{sd}})$, an additional series resistance R_s has to be considered. The measurement of R at large densities gives an estimate for $R_s \approx 2\,\mathrm{k}\Omega$ which is an order of magnitude smaller than the resistance in the gap, indicating that Δ can be estimated well from $G(V_{\mathrm{sd}})$.

The external field $D = 1/2\epsilon_0(C_{\mathrm{b}}V_{\mathrm{b}} - C_{\mathrm{t}}V_{\mathrm{t}})$ is simulated in the band structure calculation by an on-site energy difference Δ_{V} between adjacent layers, where the on-site energy from the top-most to the bottom-most layer is $U = \Delta_{\mathrm{V}}(-3/2, -1/2, 1/2, 3/2)$. The relation of Δ_{V} to the external field D for bilayer is $\Delta_{\mathrm{V}} = eDd/\epsilon = eD\epsilon_0/C_{\mathrm{BLG}}$, with $C_{\mathrm{BLG}} \approx 7.5\,\mu\mathrm{F/cm}^2$ the capacitance between the graphene layers[28]. Therefore, for the four layers, $\Delta_{\mathrm{V}} = bD$ with $b = e\epsilon_0/2C_{\mathrm{BLG}} \approx 59\,\mathrm{meV/(Vnm^{-1})}$.

For our intermediate twist angle $\theta = 2.37°$, the density of full filling of the first band ($n_{\mathrm{s}} \approx 13 \times 10^{12}\,\mathrm{cm}^{-2}$) is outside the measurement range. However, we have three possibilities to determine the twist angle. First, we do observe Landau levels emerging from the band edge, allowing us to estimate n_{s}. Second, the Lifshitz transition is clearly visible in our devices and its critical density is characteristic for a certain twist angle. Finally, the Hofstadter butterfly pattern, where we clearly observe flux quanta through up to 37 moiré unit cells, allows us to determine the size of the unit cell and therefore the twist. All three methods are explained in Ref.[26]. We find a twist angle of 2.35° with little variation (±0.04°) along the 15 μm long device.

B. Measurements in other devices

In Fig. S1 we show two terminal resistance measurements $R(V_{\mathrm{t}}, V_{\mathrm{b}})$ for different junctions on the device. A resistance peak at finite D and $n = 0$ is observed for all devices, i.e. all devices exhibit the correlated electron/hole gap.

C. Measurement at different twist angles

Here we analyze the impact of the twist angle by contrasting $R_{\mathrm{xx}}(n, D)$ and Landau fans at $\theta = 2.37°$ to measurements at $\theta = 10°$ and $\theta = 1.2°$. We first consider the large twist device, where we observe decoupled behavior. In the $R(n, D)$ map shown in Fig. S2a, a large resistance peak around $(n, D) = (0, 0)$ is measured that is attributed to the presence of crystal fields[27]. By increasing the displacement field, two features of increased resistance split up (marked with orange and blue arrows), corresponding to charge neutrality lines in the top and bottom bilayer. Importantly, around $n = 0$ no resistance peak is observed (white arrow), in agreement with the observations in Ref.[27]. The Landau fan at finite $D = -0.35\,\mathrm{V/nm}$ in Fig. S2b agrees with the expected coexistence of electron and hole bands. At large twist angles, it is therefore possible to observe the coexistence of electron and hole Fermi surfaces, but these do not form a correlated state.

Decoupled behavior and overlapping electron/hole bands are also observed for the $\theta = 2.37°$ device, Fig. 4b. In contrast to $\theta = 10°$, the single-band regions occupy a larger density range due to increased effective mass. However, the devices can be described by a similar electrostatic model. The important difference is the occurrence of a gap at $n = 0$ and finite D.

The small twist-angle device (Fig. 4c) exhibits a fundamentally different behavior (see also[19–21]). Resistance peaks are observed at $n \approx \pm 3 \times 10^{12}\,\mathrm{cm}^{-2}$ due to filling of the first band. At $D = 0$, there is no band gap at zero energy due to band overlap. The band overlap is removed by applying a displacement field $|D| > 0.3\,\mathrm{V/nm}$, where a single

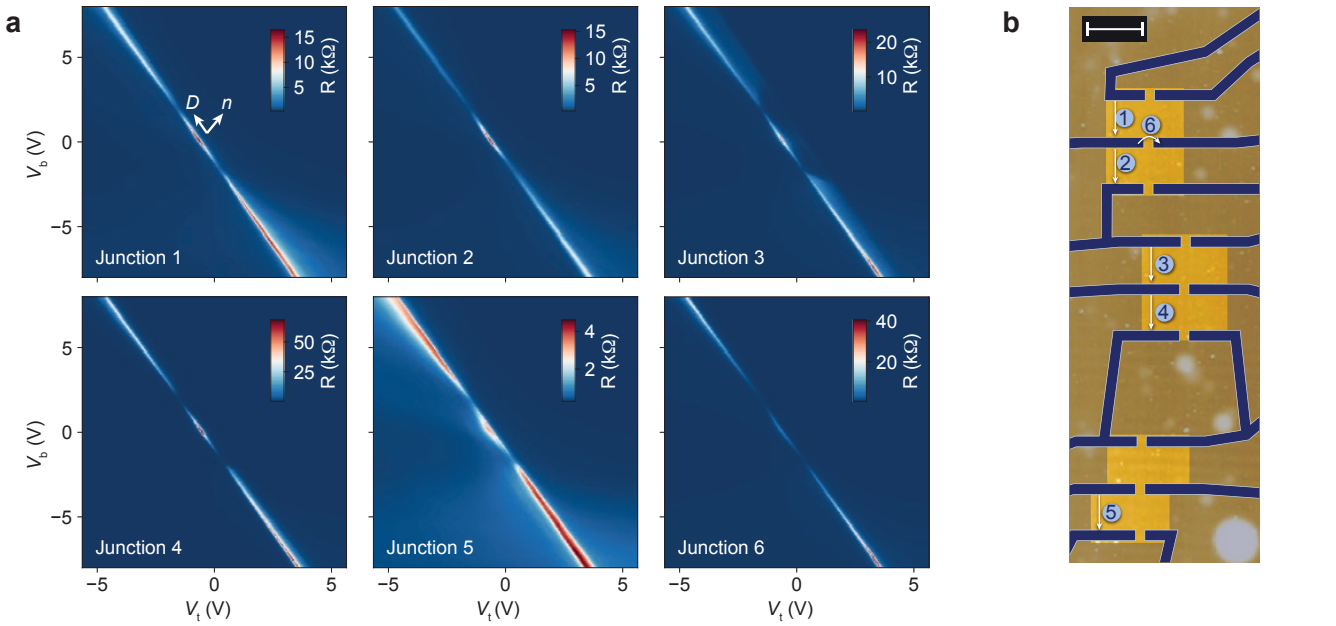

FIG. S1. a) Two-terminal resistance R as a function of top- and back gate voltage (V_t, V_b). Direction of D and n are indicated. b) Device schematics, contacts blue, etched parts brown. The junctions measured in a) are indicated with numbers. Scale-bar: 2 μm.

particle gap appears. The Landau fan in this regime reveals that electron and hole bands do not overlap at finite D, they rather emerge from the gap around $n = 0$. This is in agreement with band structure calculations that exhibit a single-particle gap at finite D[3,21]. At small twist angles it is therefore not possible to engineer a coexistence of electron and hole Fermi surfaces by increasing the displacement field. This is due to the fact that the wavefunction is no longer layer polarized, therefore it is not possible to charge the upper bilayer with electrons and the lower bilayer with holes.

The measurements strongly suggest that an intermediate twist angle is important. We argue that, on the one hand, the twist needs to be large enough such that layer-polarized, bilayer bands emerge from the κ,κ' points, see also[26]. The bilayer bands can be individually controlled by top/back gate electrodes. In strong contrast to correlated states that are formed out of flat bands, here, single-particle band structure calculations reveal the states out of which a correlated groundstate is formed. On the other hand, the twist angle needs to be small enough such that the effective mass of the bands is sufficiently large to obtain a well observable gap, as we argue in the main text.

D. Thermal activation of the gap

In Fig. S3 we show additional data on the thermal activation of the gap.

E. Effective mass

In Fig. S4 we show extracted effective masses for different cuts in the n, D map for the device at $\theta = 2.37°$. The extraction was done by analyzing the thermal activation of Shubnikov-de Haas oscillations. The average effective mass along the red and blue cut (single valence band region) is $m^* = 0.09m_e$ and $0.08m_e$, respectively. For the double band region we find, in average, $m^* = 0.06m_e$, and for the single and double counduction band region (yellow) $m^* = 0.09m_e$.

To extract the effective masses from the different regions of the $n-D$ map we remove a background from $R_{xx}(n, T)$ and obtain a series of Shubnikov-de Haas (SdH) oscillations for different temperatures, as shown in Fig. S5a. We remove a polynomial background. This is done for the minimal polynomial order and the maximal polynomial order which result in a flat background, separately. For each of the two selected extremes we perform the following procedure for extracting the effective mass: We select a peak at a given density and extract its maximum value for every different

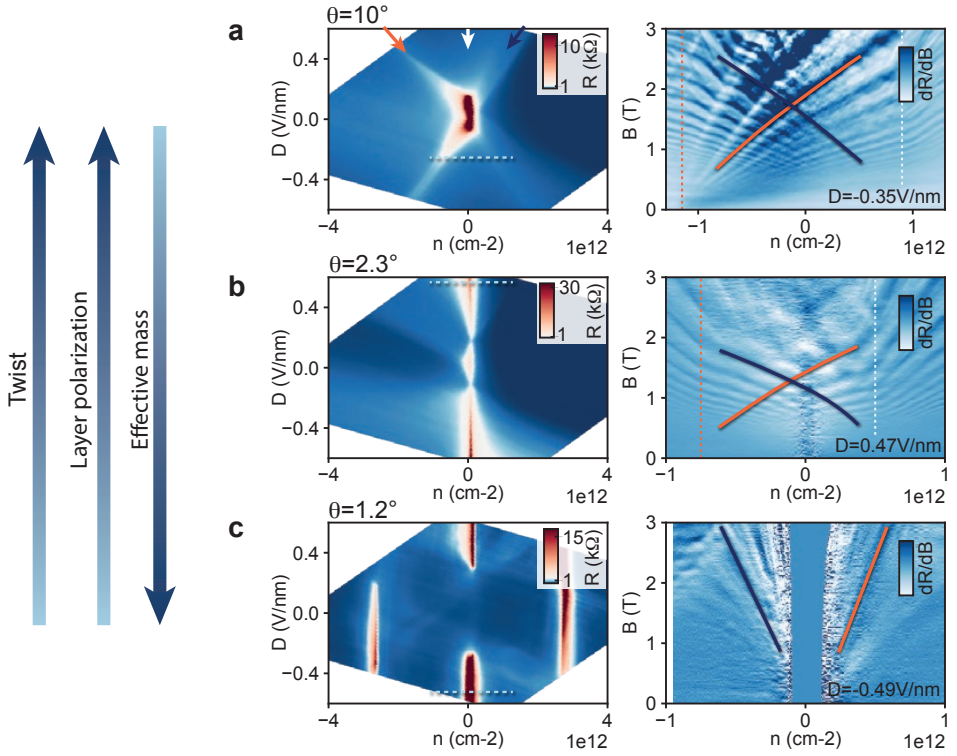

FIG. S2. Comparison of $R(n, D, B = 0)$ and Landau fans at finite D for different twist angles. For better visibility, the numerical derivative dR/dB of the Landau fan is shown. a) The large-twist angle device ($\theta = 10°$) exhibits a strong resistance peak around $(n, D) \sim (0, 0)$ due to crystal fields. At finite D and $n = 0$, the system is not gapped, even though electron and hole bands coexist as seen in the Landau fan, where electron/hole resonances are indicated with red/blue lines. They originate from the band edges, indicated with dashed lines. b) Electron/hole resonances are also observed in the Landau fans for $\theta = 2.37°$. However, for $|D| > 0.1\,\mathrm{V/nm}$ and $n = 0$, a gap is observed, as discussed in the previous figures. c) The device with a smaller twist of $\theta = 1.2°$ exhibits a fundamentally different behavior. No gap is observed at $(n, D) \sim (0, 0)$, but at $(|n|, D) \sim (3 \times 10^{12}\,\mathrm{cm}^{-2}, 0)$ (full filling of the moiré unit cell) and for $(n, |D|) \sim (0, > 0.3\,\mathrm{V/nm})$ which is due to a band-gap in the band structure at finite D. In this case, the Landau fan emerges from $n = 0$ and electron/hole resonances do not cross.

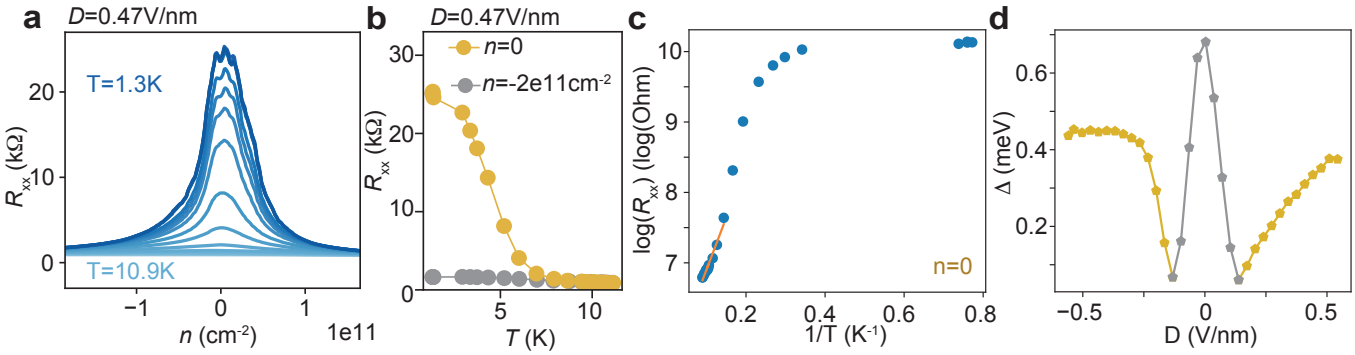

FIG. S3. Additional data on the thermal activation of the gap. a,b) The peak in R_{xx}, caused by the correlated gap, is vanishing quickly with temperature. c) Using a linear fit (orange) in the Arrhenius plot allows to extract the gap size Δ. d) Obtained Δ for different D, as in the main text.

temperature. We then perform a fit of such maxima as a function of temperature using the formula

$$\Delta R \propto \frac{\chi}{\sinh \chi} \qquad \text{with :} \quad \chi = \frac{2\pi^2 k_B T m^*}{\hbar e B}. \tag{S1}$$

Once obtained the value of the effective mass, m^*, we calculate two envelopes of equation (S1) as shown in Fig. S5b. The envelopes are selected such that only one data point is outside the envelopes for $T < 12.5K$. This is the threshold

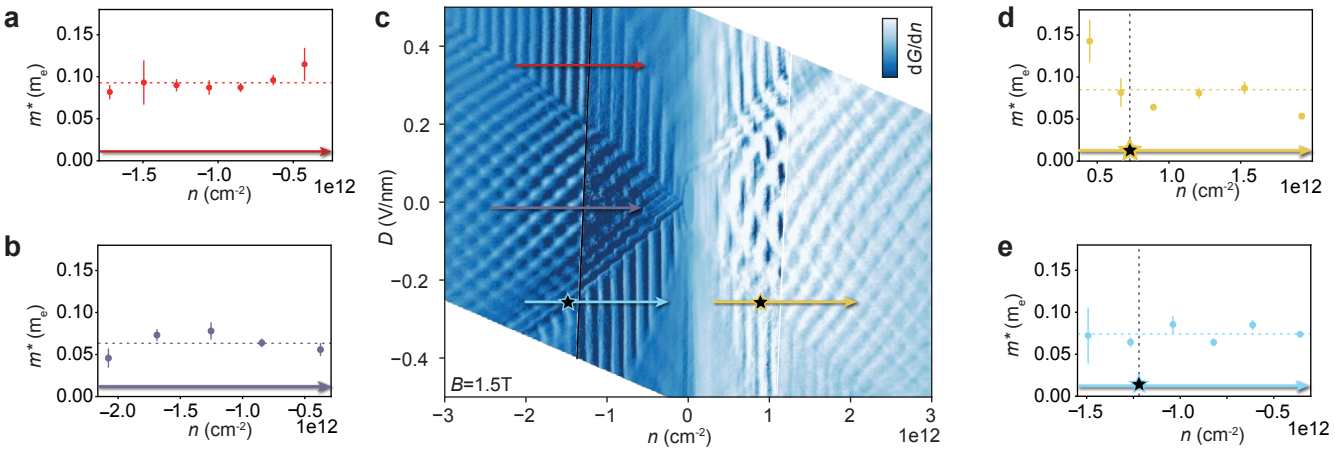

FIG. S4. a)b)d)e) Extracted effective mass for different cuts shown in c), with electron mass m_e. c) Colorscale plot of $dG/dn(n, D)$. The inner part (roughly between $\pm 1 \times 10^{12}\,\mathrm{cm}^{-2}$) is the same measurement as in Fig. 2d and we added a more coarse measurement for large densities.

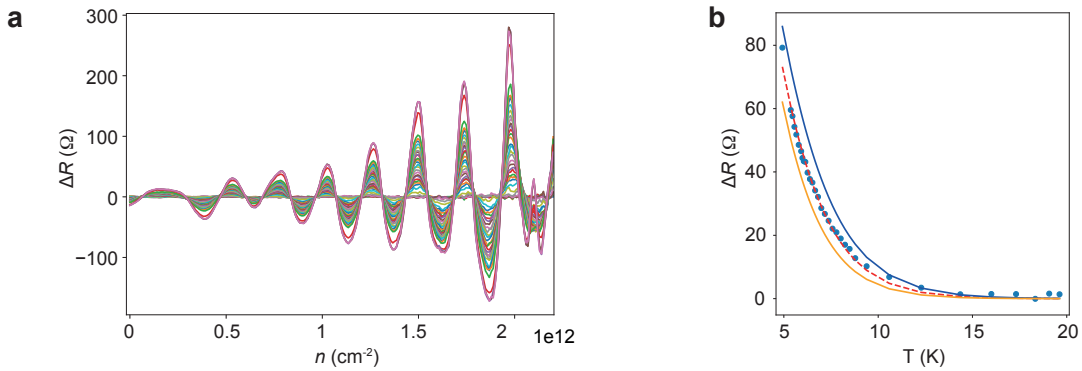

FIG. S5. a) Shubnikov-de Haas oscillations with subtracted background along a cut in Fig. S4 for temperatures between 5 and 20 K. b) $\Delta R(T)$ for a fixed density in a) where ΔR exhibits a local extrema at the lowest temperature. The data points are fitted (red dashed line) to extract the effective mass.

we use for plotting the error bars. We finally average the points of the two polynomial order extrema and merge the error bars such that we obtain the effective mass as a function of density with error bars taking into account both the background extraction and the fitting error, as shown in Fig. S4.

F. Fermi surfaces in different valleys

In Fig. S6a we show the dispersion relation at finite Δ_V in the two valleys K and K'. The corresponding Fermi-surfaces are shown in Fig. S6b at $E = 0$. With green arrows we depict two wavevectors, one corresponding to intra-valley nesting ($\mathbf{Q}_{\mathrm{intra}}$) and another corresponding to inter-valley ($\mathbf{Q}_{\mathrm{inter}}$) nesting. Since the Fermi surfaces around the κ and κ' points are not perfectly circular, it is not possible to connect the two Fermi surfaces in the same valley with the same $\mathbf{Q}_{\mathrm{intra}}$. It is, however, possible to connect the Fermi surfaces at κ and κ' between the valleys with $\mathbf{Q}_{\mathrm{inter}}$. This suggests that the correlated state is most stable when it pairs electrons and holes in opposite valleys.

At finite density and energy (Fig. S6c), not only the shape but also the size of the Fermi surfaces within the same valley and between opposite valleys becomes different, explaining the observed vanishing correlated state.

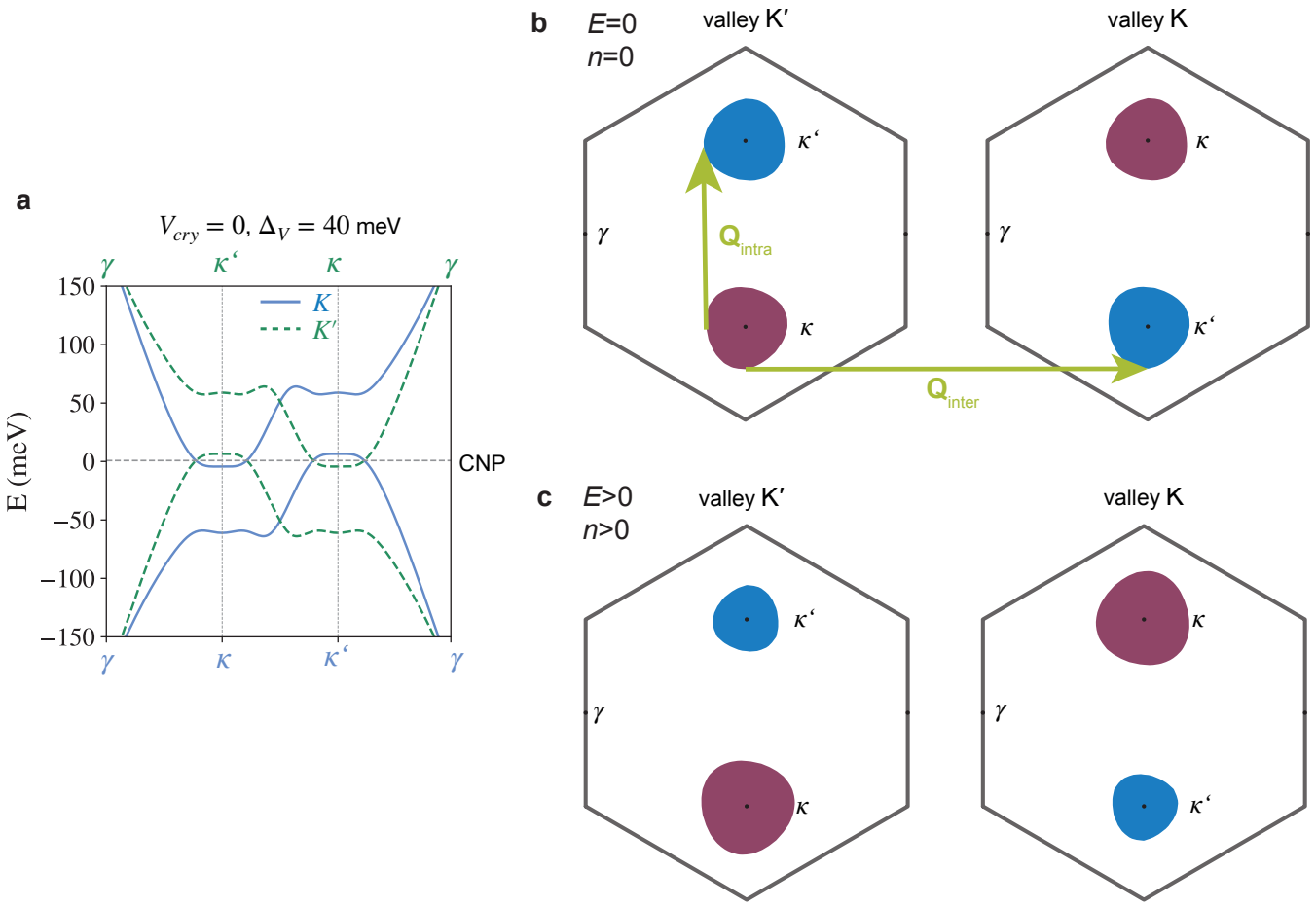

FIG. S6. a) Dispersion relation for $\Delta_V = 40\,\mathrm{meV}$ in the K (solid) and K' (dashed) valley. b) Fermi surfaces at $E = 0$ and c) $E > 0$. The green arrows show an intra- ($\mathbf{Q}_{\mathrm{intra}}$) and an inter-valley ($\mathbf{Q}_{\mathrm{inter}}$) nesting wavevector.

G. Asymmetry of the single-band regions

Consider a cut in Fig. 2e of the main text for $D = 0.3\,\mathrm{V/nm}$. The single band-region (i.e. one of the bilayers gapped) of the valence band in the top bilayer (light blue) spans a significantly larger density range than the single-band region of the conduction band in the bottom bilayer (light purple). However, in the band structure calculation in Fig. 2gh and Fig. S7b, the asymmetry seems to be opposite, i.e. the gap at κ spans a smaller energy range than the gap at κ'.

The origin of this asymmetry is closely linked to the gap that can be observed without external field ($D = 0$ or $\Delta_V = 0$ in Fig. S7). At larger twist angles, this gap is solely due to a spontaneous layer polarization of charge carriers, since the inner layers have a different electrostatic environment from the outer layers. This layer polarization has been measured and theoretically confirmed[27] at larger twist angles, but also needs to be taken into account here. In Fig. S7a and b we compare band structures without and with the crystal field contribution. Apparently, the asymmetry changes, when crystal fields are taken into account. The gap for positive energies is larger than the one for negative ones if crystal fields are considered, in contradiction with the experimental findings at $\theta = 2.37°$ but in agreement with the large twist angle device, Fig. S2a and ref.[27].

It is to be noted, however, that the band structure is also gapped if the crystal field contribution is not taken into account, see Fig. S7. Importantly, upon changing the interlayer bias Δ_V, this leads to an opposite asymmetry, counteracting the crystal field effect. We argue, that the tight-binding model may underestimate this effect. In the following, we present indications that in the experiment, the spontaneous layer polarization of charges at $D = 0$ by the moiré lattice is stronger than captured by the tight-binding model.

There are other effects that the model does not capture very accurately, e.g. the density at which the van-Hove singularity (VHS, $\sim 60\,\mathrm{meV}$ in Fig. S7a) is to be expected in the conduction and valence band. Whereas the bands for $\Delta_V = 0$ are almost perfectly electron-hole symmetric in the calculation (both with and without crystal fields), we

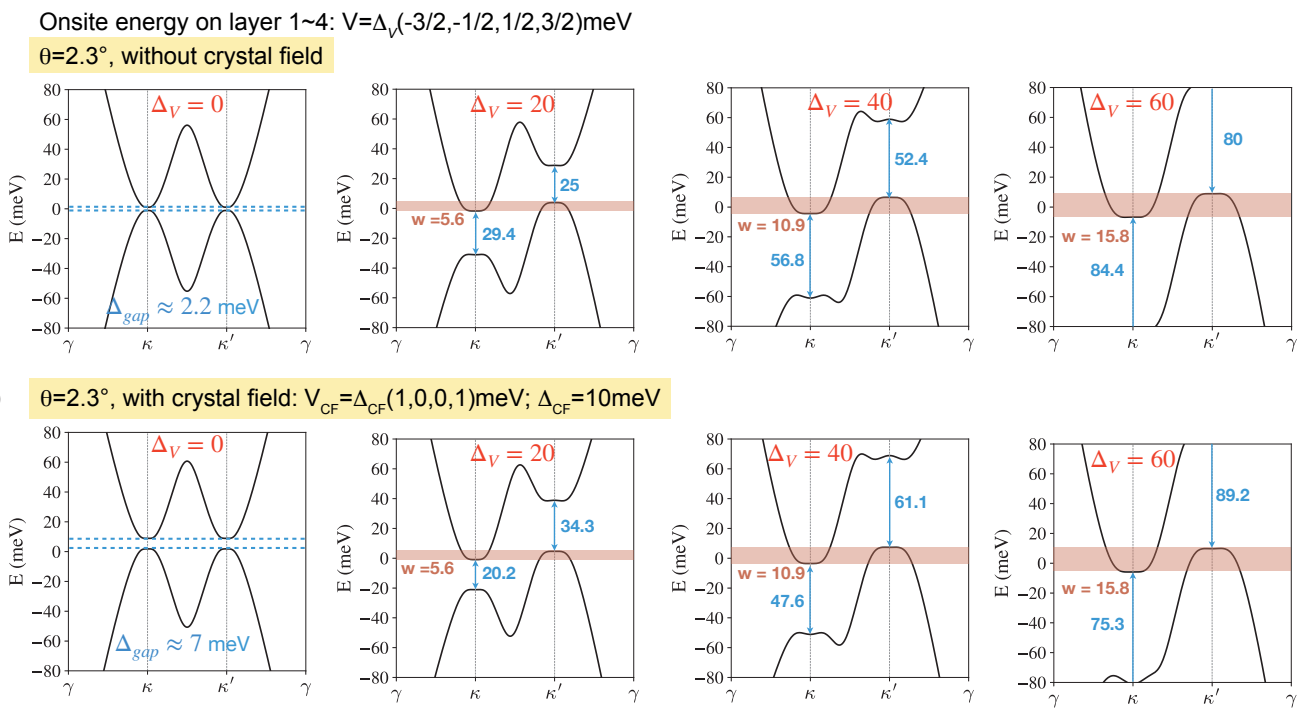

FIG. S7. Valley-projected band structures of 2.3°-TDBG for different displacement fields $D \propto \Delta_V$ using the low-energy continuum model. (a) Without crystal field contribution. (b) With the crystal field contribution.

observe a significant difference in densities of the VHS in the conduction ($n = 5.8 \times 10^{12}\,\mathrm{cm} - 2$) and valence band ($n = 5 \times 10^{12}\,\mathrm{cm} - 2$).

This qualitatively agrees with the larger effective mass that we observed for the large angle twisted bilayer device[27], where the ratio of effective masses in the valence/conduction band was $m_v/m_c \sim 1.5$ in the experiment (though with a significant error bar), $m_v/m_c \sim 1.2$ in the DFT calculation and $m_v/m_c \sim 1.1$ in the tight binding calculation[27]. We conclude that modeling the electron/hole asymmetry accurately on a quantitative level appears to be difficult using tight-binding calculations. However, the strength of the asymmetry of the gaps upon application of an interlayer bias will strongly depend on the electron/hole symmetry.

Finally, our tight binding model does not include lattice relaxation effects, which can have an impact on the asymmetry and the crystal field gap[33]. Since the energy scales of the asymmetry are rather small, a quantitative agreement between experiment and tight binding calculations is not to be expected, but not required either.

H. Electrostatic model on parabolic bands

Here we introduce a model based on parabolic bands with the goal to determine the density n and displacement field D of the transition between single- and double band regions. We start by considering the case where an external field D introduces a linear charge distribution from top to bottom layer. The electric field between the top layers, between the inner layers and between the bottom layers would be $D/3$. In contrast, if charges equilibrate completely between the inner two layers, then the displacement field in the top and bottom bilayer is $D/2$. Only in this case, the electron/hole bands at the κ and κ' point don't overlap, but touch.

We introduce the parameter p which is the probability that charges in the inner two layers equilibrate. For $p = 1$, the inner layers have the same charge density (full equilibration), for $p = 0$ the charge in the inner layers is entirely determined by the external field (no equilibration). For the field between the upper two layers, we can then write:

$$D_\mathrm{t} = \frac{D}{3-p} = \frac{1}{(3-p)2\epsilon_0}(C_\mathrm{t}V_\mathrm{t} - C_\mathrm{b}V_\mathrm{b}) \tag{S2}$$

The field between the inner layers is then

$$D_\mathrm{inner} = D(1-p)/3$$

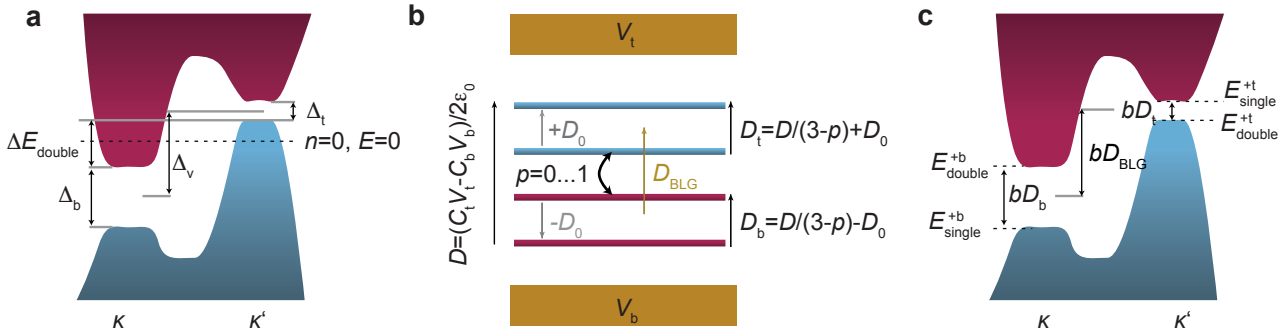

FIG. S8. Important labels of the electrostatic model. a) Sketch of a band-structure at finite displacement field. Gaps in the bottom and top-layer (Δ_t, Δ_b), band-offset Δ_v and size of the electron/hole overlap region E_double are indicated. b) Side-view of the stack where the density and field of the bilayer graphene layers (blue and red) is tuned by the voltages on the top gate V_t and the back gate V_b. The top (bottom) bilayer is exposed to a field D_t (D_b), opening a gap Δ_t (Δ_b). D_t consist of an intrinsic field D_0 and a contribution form the external field D, caused by the top/back gate voltages. D is reduced by a finite tunneling probability between the inner two layers. c) The boundaries in Fig. 2e are calculated by determining the energies of the transitions between double and single-band region in the top (t) or bottom (b) layer. For a positive displacement field $+D$, these are E^{+b}_double, E^{+t}_double, E^{+b}_single and E^{+t}_single.

For the field between the center of charges in the top and the center of charges in the bottom layer it follows:

$$D_\mathrm{BLG} = D\left(\frac{1}{3-p} + \frac{1-p}{3}\right) \tag{S3}$$

This allows to write the gap in the top and bottom bilayer and the band-offset Δ_v :

$$\Delta_\mathrm{t} = bD_\mathrm{t} + \Delta_0 \tag{S4}$$
$$\Delta_\mathrm{b} = bD_\mathrm{b} - \Delta_0 \tag{S5}$$
$$\Delta_\mathrm{v} = bD_\mathrm{BLG} \tag{S6}$$

Here, we have introduced Δ_0 to take into account the gap that is present without the application of an external field[27,33] as well as the displacement field to gap conversion factor $b = 59\,\mathrm{meV/(V/nm)}$, see Methods. The energy range of the double band region is given by $E_\mathrm{double} = \Delta_\mathrm{v} - \Delta_\mathrm{t}/2 - \Delta_\mathrm{b}/2 = \Delta_\mathrm{v} - bD/(3-p)$. We can write:

$$E_\mathrm{double} = \pm bD\left(\frac{1-p}{3}\right) =: bD\cdot f(p)$$

Note that, for $p = 1$ (full equilibration of the inner two layers), $f(p) = 0$, i.e. the bands do not overlap.
Now we need to take into account that the band-structure is gapped at zero displacement field. To enter the double band regime, a certain displacement field, D_0, needs to be applied such that the bands overlap. Therefore:

$$E^{+t}_\mathrm{double} = bf(p)\cdot(D - D_0) \qquad \text{for } D > D_0$$
$$E^{-t}_\mathrm{double} = bf(p)\cdot(D + D_0) \qquad \text{for } D < -D_0$$

The density of electrons in the double band regime is $n_\mathrm{double} = 2E_\mathrm{double}C_\mathrm{q}$, with $C_\mathrm{q} = e^2\partial n/\partial E_\mathrm{F} = e^2 2m^*/\hbar^2\pi$ for a parabolic dispersion. Starting from $E = 0$, where $n = 0$ we find:

$$n^{+t}_\mathrm{double} = C_\mathrm{q}bf(p)\cdot(D - D_0) \qquad \text{for } D > D_0 \tag{S7}$$
$$n^{+b}_\mathrm{double} = -C_\mathrm{q}bf(p)\cdot(D - D_0) \qquad \text{for } D > D_0 \tag{S8}$$
$$n^{-t}_\mathrm{double} = C_\mathrm{q}bf(p)\cdot(D + D_0) \qquad \text{for } D < -D_0 \tag{S9}$$
$$n^{-b}_\mathrm{double} = -C_\mathrm{q}bf(p)\cdot(D + D_0) \qquad \text{for } D < -D_0 \tag{S10}$$

If $\Delta_0 \approx -bf(p)D_0$, as the measurement suggests, then:

$$n^{+t}_\mathrm{double} \approx C_\mathrm{q}(bf(p)D + \Delta_0) \qquad \text{for } D > D_0 \tag{S11}$$
$$n^{+b}_\mathrm{double} \approx -C_\mathrm{q}(bf(p)D + \Delta_0) \qquad \text{for } D > D_0 \tag{S12}$$
$$n^{-t}_\mathrm{double} \approx C_\mathrm{q}(bf(p)\cdot D - \Delta_0) \qquad \text{for } D < -D_0 \tag{S13}$$
$$n^{-b}_\mathrm{double} \approx -C_\mathrm{q}(bf(p)\cdot D - \Delta_0) \qquad \text{for } D < -D_0 \tag{S14}$$

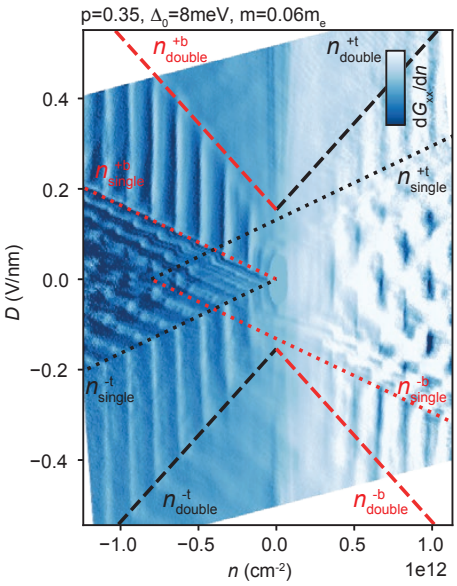

FIG. S9. Calculated lines that separate the different regions in the D vs. n map.

To reach the end of the single-band regime, $E_{\rm single}$ in the top layer:

$$E^{+t}_{\rm single} = E^{+}_{\rm double}/2 + \Delta_{\rm t}$$

In density

$$n^{+t}_{\rm single} = C_{\rm q}(E^{+}_{\rm double} + \Delta_{\rm t}) \qquad \text{for } D > D_0$$

This gives the four lines:

$$n^{+t}_{\rm single} = C_{\rm q}/e\left(bf(p)\cdot(D-D_0) + b\tilde{f}(p)D + \Delta_0\right) \qquad \text{for } D > D_0 \tag{S15}$$

$$n^{-t}_{\rm single} = C_{\rm q}/e\left(bf(p)\cdot(D+D_0) + b\tilde{f}(p)D + \Delta_0\right) \qquad \text{for } D < -D_0 \tag{S16}$$

$$n^{+b}_{\rm single} = -C_{\rm q}/e\left(bf(p)\cdot(D-D_0) + b\tilde{f}(p)D - \Delta_0\right) \qquad \text{for } D > D_0 \tag{S17}$$

$$n^{-b}_{\rm single} = -C_{\rm q}/e\left(bf(p)\cdot(D+D_0) + b\tilde{f}(p)D - \Delta_0\right) \qquad \text{for } D < -D_0 \tag{S18}$$

$$\tag{S19}$$

with:

$$f(p) = \frac{1-p}{3}, \qquad \tilde{f}(p) = \frac{1}{3-p}, \qquad g(p) = f + \tilde{f} \tag{S20}$$

If $\Delta_0 \approx -bf(p)D_0$, as the measurement suggests, then:

$$n^{+t}_{\rm single} \approx \frac{C_{\rm q}bg(p)}{e}D - \frac{2C_{\rm q}}{e}\Delta_0 \qquad \text{for } D > D_0 \tag{S21}$$

$$n^{+b}_{\rm single} \approx -\frac{C_{\rm q}bg(p)}{e}D \qquad \text{for } D > D_0 \tag{S22}$$

$$n^{-t}_{\rm single} \approx \frac{C_{\rm q}bg(p)}{e}D \qquad \text{for } D < -D_0 \tag{S23}$$

$$n^{-b}_{\rm single} \approx -\frac{C_{\rm q}bg(p)}{e}D - \frac{2C_{\rm q}}{e}\Delta_0 \qquad \text{for } D < -D_0 \tag{S24}$$

$$\tag{S25}$$

The results are plotted in Fig. S9.

I. Zeeman splitting

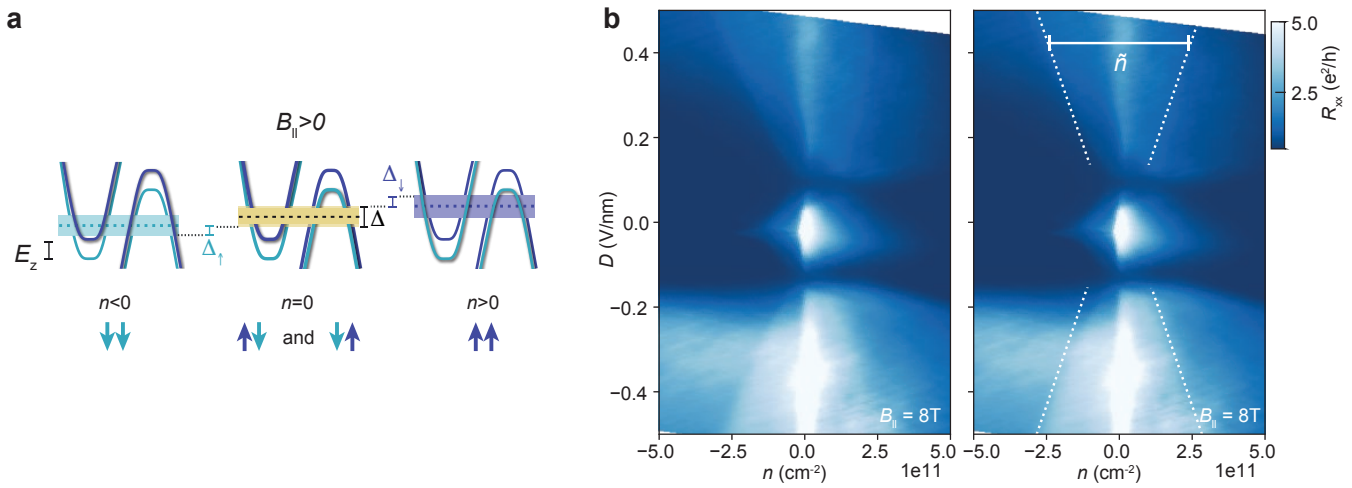

FIG. S10. a) Schematics of band structures and gap formation at different n in finite $B_\parallel$ (compare to Fig. 3e). b) Experimental data without and with fits that determine the expected boundary of the single-spin region (compare to Fig. 3g). Dashed lines are coarse fits. The width $\tilde{n}$ of the single-spin region depends on the gap size which scales with D.

In the main text we discuss that, at $n = 0$, a correlated gap out of opposite magnetic moments can be formed. We now calculate the density $\tilde{n}$ that determines the boundaries of these three gapped regions as a function of $B_\parallel$ and D (see Fig. S10b).

By applying a parallel magnetic field $B_\parallel$, The energy of bands with different magnetic moments shift by the Zeeman energy $E_z = g\mu_B B_\parallel$, with $g = 2$ in graphene. We label the regions where only one spin band is gapped as $\Delta_\uparrow$ and $\Delta_\downarrow$ (see Fig. S10a). The size of these regions is given by the Zeemann energy $\Delta_\uparrow + \Delta_\downarrow = E_z$. The energy range of the band structure that is partially or entirely gapped is therefore $E_z + \Delta$, where Δ corresponds to the gap size at $n = 0$. We thus obtain $\tilde{n}$:

$$\tilde{n} = \frac{C_q}{e^2}(2\Delta + E_z) \tag{S26}$$

where $C_q = e^2 \cdot 2m^*/(\hbar^2\pi)$ for a parabolic bilayer band. When converting gap to density, Δ has to be multiplied by 2 since all the bands are gapped there, as opposed to the single-spin gapped regions (see Fig. S10).

To obtain the coarse fits we estimate $\Delta(D, B_\parallel)$ from the experiment. In Fig. 3b we can roughly fit the size of the correlated gap:

$$\Delta(D, B_\parallel = 0) = \alpha(D - D_0) \tag{S27}$$

with $\alpha = 15\,\mathrm{meV/(Vnm^{-1})}$ and $D_0 = 0.15\,\mathrm{V/nm}$. From bias measurements at $n = 0$ as a function of $B_\parallel$ (Fig. S11) we find that $\Delta(B_\parallel = 8\,\mathrm{T})/\Delta(B_\parallel = 0) \approx 1/2$. We thus obtain $\tilde{n}(D, B_\parallel = 8\,\mathrm{T})$. With $m^* = 0.12m_e$ we obtain the dashed line shown in Fig. S10b.

J. Gap in parallel magnetic field

Here we show additional data in parallel magnetic field. In Fig. S11a we show the gap in a V_{sd} measurement as a function of density and for $B_\parallel = 0$ and $B_\parallel = 4\,\mathrm{T}$. As a guide, we mark the corresponding lines in the R_{xx} map (Fig. S11 and Fig. 3f). The source drain measurement exhibits a reduced conductance at $B_\parallel = 4\,\mathrm{T}$ between the region, marked by red arrows, which is not present at $B_\parallel = 0$. We attribute this to a partially gapped band structure, as argued previously.

In Fig. S11c, we show the evolution of the gap with $B_\parallel$ at $D = 0.47\,\mathrm{V/nm}$ and $n = 0$ in a V_{sd} waterfall plot. With increasing $B_\parallel$, the feature that we identify as the main gap is reduced in energy. This is consistent with the Zeeman-split spin bands (Fig. S10a), where two gaps of different size emerge for the two possibilities of spin pairing at $n = 0$. Note that in the bias measurement, the region where all spin bands are gapped (given by the size of the smallest gap) leads to the most significant decrease of conductance. I.e. the gap that is observed in Fig. S11c corresponds to the smaller gap at $n = 0$, which is decreasing with $B_\parallel$.

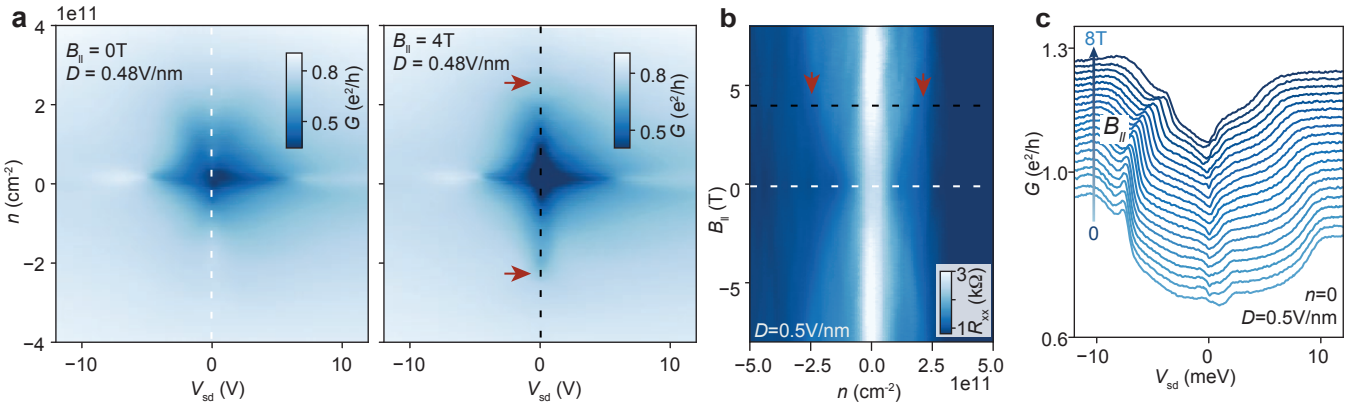

FIG. S11. a) $G(V_{\rm sd}, n)$ at large D for $B_\parallel = 0$ and $B_\parallel = 4\,$T. With red arrows we mark the end of the single-band region that occurs due to Zeeman splitting. b) As a comparison, we mark this region also in $R_{\rm xx}(n, B_\parallel)$, as well as the corresponding cuts in a) c) Gap in $G(V_{\rm sd})$ as a function of $B_\parallel$.

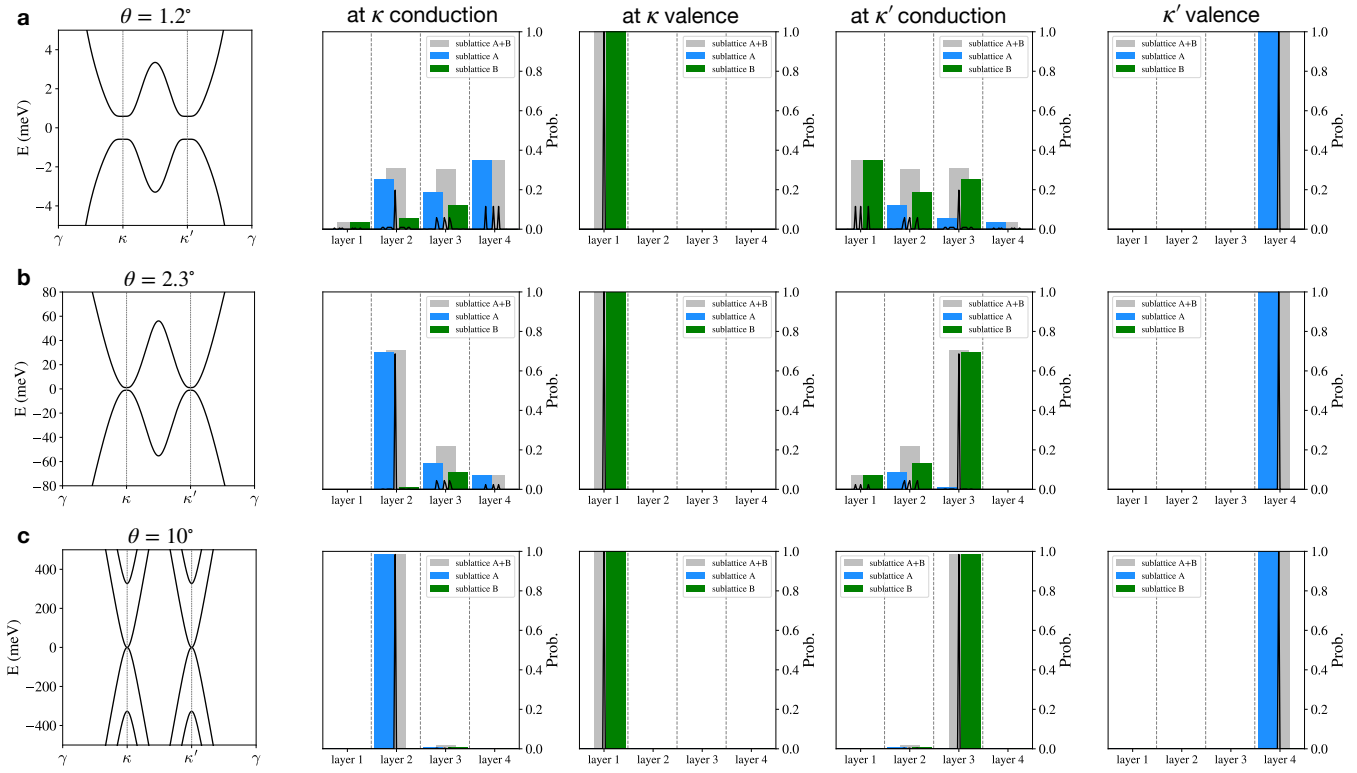

FIG. S12. Band structures and probabilities at κ and κ' of the first conduction and valence bands. (a) $\theta = 1.2°$, (b) $\theta = 2.3°$, (c) $\theta = 10°$. For small twist angles, the middle two graphene layers are strongly coupled thereby decreasing the layer polarization. For $\theta \gtrsim 2°$, the wave function is mainly localized on a specific sublattice and a moiré reciprocal lattice vector $\mathbf{G}_0 = 0$ (indicated by the sharp peak).

K. Layer polarization and effective mass

We show band structures and probabilities at κ and κ' for twist angles 1.2°, 2.3° and 10° in Fig. S12, where crystal fields and external electric fields are ignored. As the twist angle increases, electrons are concentrated on layer 2 at κ and on layer 3 at κ'. Here layer 1 to 4 denote top-most layer to bottom-most layer. Since the probabilities of valence bands do not change with respect to twist angles, we define the layer polarization as the probability on the top bilayer (layer 1,2) at κ, i.e. Prob($\kappa_{\rm top}$).

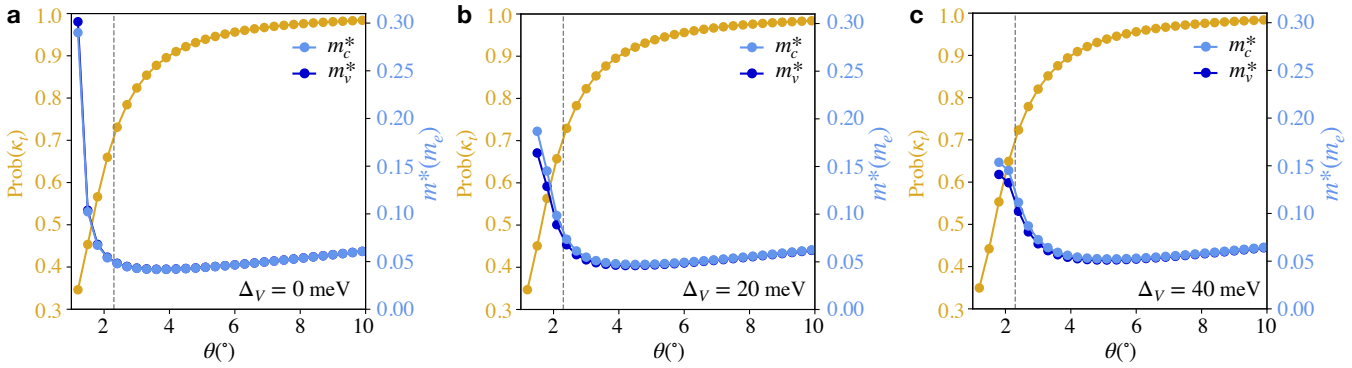

FIG. S13. Layer polarization Prob(κ_t) and effective mass m^* in units of free electron mass m_e with respect to twist angle. m_c^* (m_v^*) is the effective mass of conduction (valence) band near κ (κ'). The vertical dashed line is a guide to the eye at $\theta = 2.3°$, which is the relevant angle in our experiment and theoretical calculations. (a) $\Delta_V = 0$ meV, (b) $\Delta_V = 20$ meV, (c) $\Delta_V = 40$ meV. At some finite Δ_V, both layer polarization and effective mass are large near $\theta \sim 2°$. This explains our observation of the excitonic insulating state only near an intermediate twist angle $\sim 2°$.

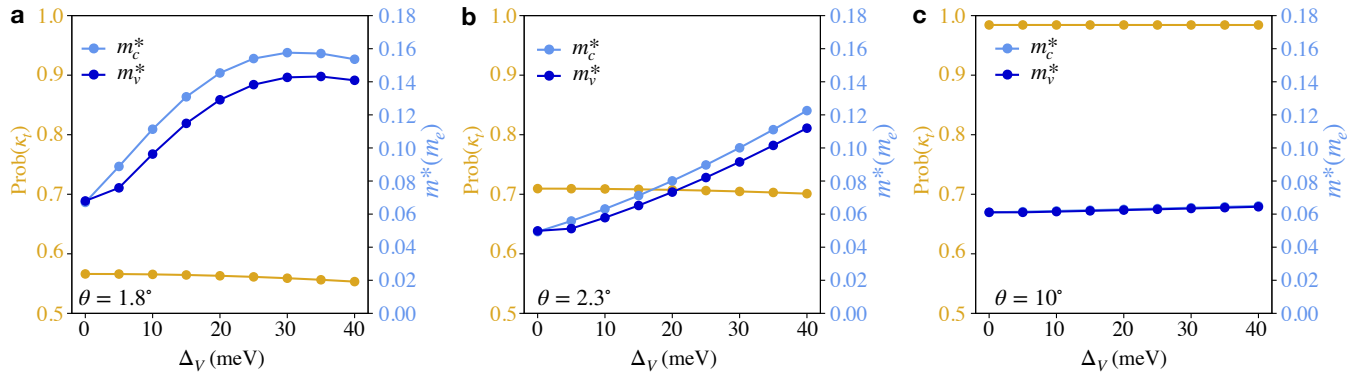

FIG. S14. Layer polarization Prob(κ_t) and effective mass m^* in units of free electron mass m_e for different twist angles. (a) $\theta = 1.8°$, (b) $\theta = 2.3°$, (c) $\theta = 10°$.

To qualitatively capture the band flatness near the Fermi level, we estimate the effective mass m^* by

$$m^* = \frac{\hbar^2(k-\kappa)^2}{2m_e(E_k - E_\kappa)} \tag{S28}$$

and k is taken to be $|\kappa' - \kappa|/4$ away from the reference point κ.

Figure S13 shows the layer polarization Prob(κ_t) and effective masses of conduction band m_c^* and valence band m_v^* as a function of twist angle for external fields $\Delta_V = 0$, $\Delta_V = 20$ meV and $\Delta_V = 40$ meV. m_c^* (m_v^*) is estimated near κ (κ') as defined in Eq.(S28). The layer polarization increases quickly with twist angle and does not evidently depend on external field Δ_V. On the contrary, the effective masses decrease quickly with twist angle and the steepness depends on Δ_V. At some finite Δ_V, the situation is optimized near $\theta \sim 2°$ where both layer polarization and effective mass are large. This explains our observation of the excitonic insulating state only near an intermediate twist angle near 2°.

The layer polarization and effective masses as a function of displacement field parameter Δ_V for $\theta = 1.8°$, 2.3° and 10° are shown in Fig. S14. As we pointed out in the main text, the layer polarization is almost independent of Δ_V. For large twist angle, for example 10° in Fig. S14c, effective masses m_c^* and m_v^* are the same and independent of Δ_V. This indicates high symmetry between conduction and valence band. For intermediate twist angles, for example 2.3° in Fig. S14b, both layer polarization and effective masses are relatively large, which is close to the optimal situation to realize the excitonic insulator. For small twist angles, for example 1.8° in Fig. S14a, the layer polarization is small even though the effective mass is large. For intermediate twist angles, m_c^* and m_v^* differs by an amount which is increasing with Δ_V, this partly explains the correlated gap decreasing for large Δ_V as in Fig. 4c as a result of asymmetric bands.

L. Self-consistent Hartree Fock using an effective two-band model

In Fig. S12b, we have shown that the low-energy bands of $\theta = 2.3^\circ$ near Fermi level at charge neutrality mainly localize on the middle two graphene layers on a specific sublattice and a moiré reciprocal lattice vector $\mathbf{G}_0 = 0$. We, therefore, can map the Hamiltonian to a 2×2 effective Hamiltonian using the partition technique developed by Feshbach[34] and Lowdin[35]. We divide the Hilbert space of TDBG into two parts, target subspace and background subspace with subscripts t and b respectively:

$$H = \begin{pmatrix} H_t & H_{tb} \\ H_{bt} & H_b \end{pmatrix} \tag{S29}$$

After mapping, the effective Hamiltonian in the target subspace H_t^{eff} keeps the same eigenvalues and eigenvectors as H:

$$H_t^{\text{eff}} = H_t + H_{tb}(\varepsilon_n - H_b)^{-1} H_{bt} \tag{S30}$$

where ε_n is eigenvalue of the original Hamiltonian H.

The basis of 2×2 effective Hamiltonian H^{eff} of TDBG is $(z_{A2,\mathbf{G}_0} \;\; z_{B3,\mathbf{G}_0})^T$, where 2 and 3 are layer indices, A and B are sublattices and moiré reciprocal lattice vector $\mathbf{G}_0 = 0$. The Coulomb interaction of this two-band model is

$$V = \frac{1}{2A} \sum_{\mathbf{k},\mathbf{k}',\mathbf{q}} \left(V_q^S a^\dagger_{c,\mathbf{k}+\mathbf{q}} a^\dagger_{c,\mathbf{k}'-\mathbf{q}} a_{c,\mathbf{k}'} a_{c,\mathbf{k}} + V_q^S a^\dagger_{v,\mathbf{k}+\mathbf{q}} a^\dagger_{v,\mathbf{k}'-\mathbf{q}} a_{v,\mathbf{k}'} a_{v,\mathbf{k}} \right) + \frac{1}{A} \sum_{\mathbf{k},\mathbf{k}',\mathbf{q}} V_q^D a^\dagger_{c,\mathbf{k}+\mathbf{q}} a^\dagger_{v,\mathbf{k}'-\mathbf{q}} a_{v,\mathbf{k}'} a_{c,\mathbf{k}} \tag{S31}$$

where c and v denote conduction and valence band respectively. The Coulomb potential in the same layer is $V_q^S = \frac{2\pi e^2}{\epsilon q}$, and the Coulomb potenial between different layers is $V_q^D = \frac{2\pi e^2}{\epsilon q} e^{-qd}$. In the Hartree Fock mean-field theory, the total Hamiltonian is

$$H_{\text{MF}} = H^{\text{eff}} + V_{\text{MF}} = \sum_{\mathbf{k}} \begin{pmatrix} a^\dagger_{c\mathbf{k}} & a^\dagger_{v\mathbf{k}} \end{pmatrix} \begin{pmatrix} \varepsilon_{c\mathbf{k}} & -\Delta_{\mathbf{k}} \\ -\Delta^*_{\mathbf{k}} & \varepsilon_{v\mathbf{k}} \end{pmatrix} \begin{pmatrix} a_{c\mathbf{k}} \\ a_{v\mathbf{k}} \end{pmatrix} \tag{S32}$$

A set of equations are solved self consistently:

$$\varepsilon_{c\mathbf{k}} = \varepsilon^0_{c\mathbf{k}} + \frac{2\pi \varepsilon^0_{c\mathbf{k}} e^2 d n_e}{\epsilon} - \frac{1}{A} \sum_{\mathbf{k}'} V^S(\mathbf{k}' - \mathbf{k}) \langle a^\dagger_{c\mathbf{k}'} a_{c\mathbf{k}'} \rangle \tag{S33}$$

$$\varepsilon_{v\mathbf{k}} = \varepsilon^0_{v\mathbf{k}} - \frac{2\pi e^2 d n_h}{\epsilon} - \frac{1}{A} \sum_{\mathbf{k}'} V^S(\mathbf{k}' - \mathbf{k}) \left(\langle a^\dagger_{v\mathbf{k}'} a_{v\mathbf{k}'} \rangle - 1 \right) \tag{S34}$$

$$\varepsilon_{\mathbf{k}} = \frac{1}{2}(\varepsilon_{c\mathbf{k}} - \varepsilon_{v\mathbf{k}}) \tag{S35}$$

$$\Delta_{\mathbf{k}} = \frac{1}{A} \sum_{\mathbf{k}'} V^D(\mathbf{k}' - \mathbf{k}) \frac{\Delta_{\mathbf{k}'}}{2\sqrt{\varepsilon^2_{\mathbf{k}'} + \Delta^2_{\mathbf{k}'}}} \tag{S36}$$

$$n_e = \frac{1}{A} \sum_{\mathbf{k}} \langle a^\dagger_{c\mathbf{k}} a_{c\mathbf{k}} \rangle \tag{S37}$$

where $\varepsilon^0_{c\mathbf{k}}$ and $\varepsilon^0_{v\mathbf{k}}$ are eigenvalues of H^{eff}.

M. Static polarization function and dielectric constant

The electric field modifies the band structure, especially the band gaps of top and bottom bilayers as shown in Fig. S7, thereby the static dielectric constant. We examine the static polarization function using the Lindhard formula

$$\Pi_0^{\mathbf{G}\mathbf{G}'}(\mathbf{q}, \omega \to 0) = \frac{g}{A} \sum_{\substack{n,m,\mathbf{k} \\ \mathbf{G}_1,\mathbf{G}_2}} \frac{f(\varepsilon_{n,\mathbf{k}}) - f(\varepsilon_{m,\mathbf{k}+\mathbf{q}})}{\varepsilon_{n,\mathbf{k}} - \varepsilon_{m,\mathbf{k}+\mathbf{q}}} \langle \psi_{n,\mathbf{k}+\mathbf{G}_1} | e^{-i(\mathbf{q}+\mathbf{G})\cdot\mathbf{r}} | \psi_{m,\mathbf{k}+\mathbf{q}+\mathbf{G}_1} \rangle \langle \psi_{m,\mathbf{k}+\mathbf{q}+\mathbf{G}_2} | e^{i(\mathbf{q}+\mathbf{G}')\cdot\mathbf{r}} | \psi_{n,\mathbf{k}+\mathbf{G}_2} \rangle \tag{S38}$$

$\mathbf{G}$, $\mathbf{G}'$, $\mathbf{G}_1$ and $\mathbf{G}_2$ are moiré reciprocal lattice vectors, $\mathbf{k}$ and $\mathbf{q}$ are in the first moiré Brillouin zone, A is area, $g = 4$ includes spin and valley degeneracies.

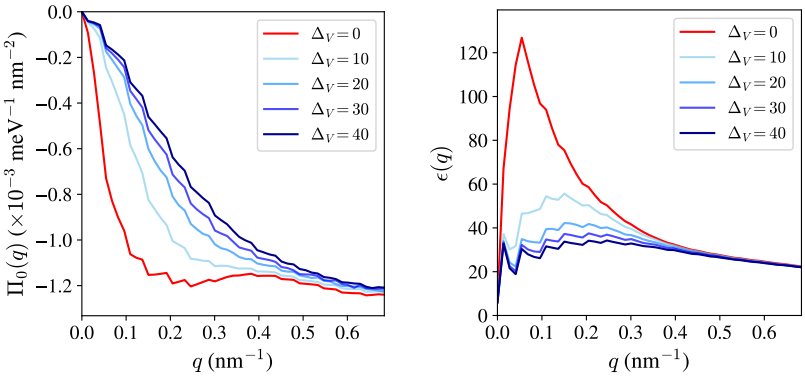

FIG. S15. Static polarization function $\Pi_0(q)$ and dielectric function $\epsilon(q)$ of 2.3°-TDBG for different displacement fields $\Delta_{\mathrm{V}} = 0 - 40$ meV. The dielectric function decreases with Δ_{V}.

The characteristic wavelength of the Fermi surface near charge neutrality is much longer than the moiré period, we can therefore consider only the polarization function matrix element of $\mathbf{G} = \mathbf{G}' = 0$:

$$\Pi_0(\mathbf{q}) = \frac{g}{A} \sum_{\substack{n,m,\mathbf{k} \\ \mathbf{G}_1,\mathbf{G}_2}} \frac{f(\varepsilon_{n,\mathbf{k}}) - f(\varepsilon_{m,\mathbf{k}+\mathbf{q}})}{\varepsilon_{n,\mathbf{k}} - \varepsilon_{m,\mathbf{k}+\mathbf{q}}} \langle \psi_{n,\mathbf{k}+\mathbf{G}_1} | e^{-i\mathbf{q}\cdot\mathbf{r}} | \psi_{m,\mathbf{k}+\mathbf{q}+\mathbf{G}_1} \rangle \langle \psi_{m,\mathbf{k}+\mathbf{q}+\mathbf{G}_2} | e^{i\mathbf{q}\cdot\mathbf{r}} | \psi_{n,\mathbf{k}+\mathbf{G}_2} \rangle \tag{S39}$$

and the static dielectric constant stemmed from the interband transitions is

$$\epsilon_i(\mathbf{q}) = 1 - \frac{V(\mathbf{q})}{\epsilon_b} \Pi_0(\mathbf{q}) \tag{S40}$$

$V(\mathbf{q})$ is the bare Coulomb potential and ϵ_b is the background dielectric constant coming from surrounded dielectrics. In TDBG encapsulated by hBN substrates, we use $\epsilon_b = 6$ for hBN. The total dielectric constant incorporated in self-consistent Hartree Fock calculation is

$$\epsilon(\mathbf{q}) = \epsilon_b - V(\mathbf{q}) \Pi_0(\mathbf{q}) \tag{S41}$$

We show the static polarization function $\Pi_0(q)$ and dielectric constant $\epsilon(q)$ of 2.3°-TDBG for different Δ_{V} in Fig. S15.